Direct Demonstration of the Presence of Coordinated Sulfate in the Reaction Pathway of Arabidopsis thaliana Sulfite Oxidase Using 33 S Labeling and ESEEM Spectroscopy

7 AUTHORS, INCLUDING:

Kayunta johnson-winters

University of Texas at Arlington

19 PUBLICATIONS **369** CITATIONS

SEE PROFILE

Arnold M Raitsimring

The University of Arizona

123 PUBLICATIONS **2,578** CITATIONS

SEE PROFILE

Direct demonstration of the presence of coordinated sulfate in the reaction pathway of *Arabidopsis thaliana* sulfite oxidase using [33]S labeling and ESEEM spectroscopy

Andrei V. Astashkin[†,*], **Kayunta Johnson-Winters**[†], **Eric L. Klein**[†], **Robert S. Byrne**[‡], **Russ Hille**[‡], **Arnold M. Raitsimring**[†], and **John H. Enemark**[†,*]

† *Department of Chemistry, University of Arizona, Tucson, Arizona 85721-0041*

‡ *Department of Biochemistry, University of California, Riverside, CA 92521*

Abstract

Sulfite oxidase from *Arabidopsis thaliana* has been reduced at pH = 6 with sulfite labeled with [33]S (nuclear spin $I = 3/2$), followed by reoxidation by ferricyanide to generate the Mo(V) state of the active center. To obtain information about the hyperfine interaction (*hfi*) of [33]S with Mo(V), continuous wave EPR and electron spin echo envelope modulation (ESEEM) experiments have been performed. The interpretation of the EPR and ESEEM spectra was facilitated by a theoretical analysis of the nuclear transition frequencies expected for the situation of the nuclear quadrupole interaction being much stronger than the Zeeman and hyperfine interactions. The isotropic *hfi* constant of [33]S determined in these experiments was about 3 MHz, which demonstrates the presence of coordinated sulfate in the sulfite-reduced low-pH form of the plant enzyme.

Introduction

Sulfite oxidizing enzymes occur in animals, plants, and certain bacteria. X-ray structure determinations on sulfite oxidase (SO) from chicken,[1] plant (*Arabidopsis thaliana* (At-SO)),[2] and sulfite dehydrogenase (SDH) from *Starkeya novella*,[3] show that all have nearly identical five-coordinate square pyramidal catalytic Mo-centers. In the oxidized resting state each Mo (VI) is coordinated by three equatorial sulfur atoms, two from the ubiquitous pyranopterindithiolate (molybdopterin) unit and one from a cysteinyl side chain, and by axial and equatorial oxo ligands.

The first step in the proposed catalytic cycle of SO and SDH[4–6] is the two-electron oxidation of sulfite to sulfate accompanied by reduction of Mo(VI) to Mo(IV) (Species 1 in Scheme 1). In wild-type vertebrate SO and SDH, hydrolysis of (1) to release the SO_4^{2-} product precedes one-electron oxidation to give the EPR-detectable Mo(V) form of the enzyme, Species 2. Previous EPR studies of the Mo(V) forms of vertebrate SO show that the equatorial oxo ligand in Species 2 is converted to an -OH_n group ($n = 1$ or 2) at all pH values.[7] However, in buffers that contain phosphate or arsenate, EPR and X-ray absorption spectroscopy show that the -OH_n ligand is substituted by the respective oxy-anion.[8,9]

The Mo(V) state of SO can also be generated by using one-electron reductants. For vertebrates the structure of the Mo(V) center is independent of the method of reduction.[10] However, our previous studies of At-SO[11] showed that the structure of the Mo(V) center at pH = 6 depended

CORRESPONDING AUTHOR FOOTNOTE Andrei V. Astashkin (Phone 520 621-9968; Fax 520 621-8407), John H. Enemark (Phone 520 621-2245; Fax 520 626-8065) andrei@u.arizona.edu, jenemark@u.arizona.edu.

upon the method of reduction. Reduction by Ti(III) citrate (a one-electron reductant) produced a Mo(V) center similar to SOs of vertebrates at low pH (Species 3 in Scheme 1). In contrast, if the Mo(V) state of At-SO was generated at low pH by addition of sulfite (a two-electron reductant), followed by one-electron oxidation with ferricyanide (since At-SO does not contain an intrinsic heme center, an external oxidant is needed to generate Mo(V) from Mo(IV), see Scheme 1), then no exchangeable nearby protons were observed. From comparison of the crystal structures of At-SO[2] and chicken SO,[1] we hypothesized that a change in the conformation of Arg374 near the Mo center of At-SO may result in "closed" or "open" forms of the active site that differ in the degree of accessibility of the Mo center to substrate and water molecules. It was suggested that sulfite-reduced low pH (*lpH*) At-SO is in the "closed" form with sulfate coordinated to Mo(IV). Reoxidation to Mo(V) by ferricyanide leaves the sulfate ligand trapped at the active site, and consequently, there are no ligands with exchangeable protons (Species 4 in Scheme 1). If this hypothesis could be proved for the Mo(V) center of At-SO, it would provide a rare opportunity for deeper insight into the mechanism of SO by capturing a hypothesized transient intermediate of the catalytic cycle. Typically, information about transient Mo(V) species requires rapid freeze-quench methods or other specialized procedures (see, *e.g.* 12).

Direct detection of coordinated sulfate by EPR is not possible for naturally abundant sulfur (94.93% ^{32}S, $I = 0$). However, reaction of At-SO with sulfite labeled with ^{33}S ($I = 3/2$) should result in a hyperfine interaction (*hfi*) of Mo(V) with ^{33}S, if an intermediate Mo(V)-O^{33}SO$_3$ species is produced and "trapped". By this reasoning, we have generated the *lpH* Mo(V) form of At-SO using sulfite labeled with ^{33}S and applied a variety of EPR techniques to prove the presence of ^{33}S in the Mo(V) coordination sphere. The results are reported below.

Experimental Section

Recombinant wild-type At-SO was expressed and purified as previously described.[13] To prepare Na$_2$^{33}SO$_3$, 5.0 mg of elemental sulfur (^{33}S,(99 atom %, Cambridge Isotope Laboratories) was carefully weighed into a 2.0 cm × 0.2 cm quartz tube. The tube containing ^{33}S was placed into a reaction vessel constructed from a quartz cylinder (D = H = 3 cm) with hemispherical caps. Each cap had a radius of 1.5 cm, and one cap was open to a cylindrical neck of 0.5 cm × 3.5 cm. The reaction vessel was fully evacuated and then filled with pure oxygen (0.3 atm). The neck was flame sealed, and the sealed reaction vessel was heated to 1100 °C for two minutes in a preheated tube furnace, resulting in the complete combustion of the ^{33}S and formation of ^{33}SO$_2$ (99.9%, as confirmed by GC-MS). The reaction vessel was then removed from the furnace, allowed to cool to room temperature, and opened by cracking the neck. A rubber septum was immediately attached to the neck and a solution of sodium carbonate monohydrate (18.8 mg in 379 μL of nanopure water) was added as rapidly as possible to the reaction vessel in a single portion via syringe. The mixture was vortexed for 10 minutes. The resulting solution of 400 mM Na$_2$^{33}SO$_3$ was characterized using Quantofix® sulfite test strips and was stored at −30 °C prior to use.

Two samples of At-SO were prepared for EPR investigations from the same batch of protein. One was reduced by Na$_2$^{33}SO$_3$ and another by naturally abundant Na$_2$^{32}SO$_3$. These samples will be referred to as ^{33}S-At-SO and ^{32}S-At-SO, respectively. The procedure of sample preparations was strictly the same in both cases; the protein was reduced with a 30-fold excess of sodium sulfite and then re-oxidized by about 1/2 equivalent of ferricyanide (per enzyme) to maximize the Mo(V) EPR signal. The samples were frozen in liquid nitrogen immediately after the addition of ferricyanide. The resulting concentration of Mo(V) estimated using CW EPR was about 0.4 mM.

Continuous wave (CW) X-band EPR measurements were performed on a Bruker ESP 300E spectrometer at 77 K. The electron spin echo envelope modulation (ESEEM) experiments were performed on a home-built K_a-band pulsed EPR spectrometer14 at a microwave (mw) operational frequency of about 29 GHz. Two types of ESEEM techniques were employed, two-pulse ESEEM and hyperfine sublevel correlation (HYSCORE) spectroscopy. Detailed experimental parameters are shown in the Figure legends. In all pulsed EPR experiments the measurement temperature was about 20 K. The numerical simulations of the ESEEM spectra were performed using the program SimBud (see http://quiz2.chem.arizona.edu/epr for details).

EPR-related theoretical considerations for ^{33}S

1. Expected spectroscopic parameters for ^{33}S-labeled sufate ligand—In this work, we apply CW EPR and ESEEM spectroscopy to study the hyperfine interactions of ^{33}S in order to verify the presence of an equatorial sulfate ligand at the molybdenum center of At-SO. To facilitate understanding of the experimental results, we will discuss in this section the expected magnitudes of the *hfi* and nuclear quadrupole interaction (*nqi*), and present a relevant theoretical background for analysis of the EPR and ESEEM spectra.

The expected *hfi* parameters for ^{33}S in coordinated sulfate can be estimated from comparison with the data available in the literature for ^{31}P and ^{75}As in the phosphate and arsenate ligands to the Mo(V) center of vertebrate SO. In the phosphate case, the average isotropic *hfi* constant, a_{iso}, was found to be about 10 MHz, while the anisotropic *hfi* constant was estimated as $|T_\perp|$ ~ 1 MHz.[8] In the arsenate case, a_{iso} ~ 18 MHz and $T_\perp$ ~ 3.6 MHz were found.[9] Assuming the hybridizations of the valence shell electronic orbitals for sulfur in sulfate, phosphorus in phosphate, and arsenic in arsenate to be nearly the same and essentially sp^3, one can simply use the ratios of atomic *hfi* constants, a_{33S}/a_{31P} ~ 0.26 and a_{33S}/a_{75As} ~ 0.29,[15] to estimate a_{iso} ~ 4 – 6 MHz for ^{33}S in a sulfate ligand.

The situation with the anisotropic *hfi* is somewhat more complex because it has contributions from the spin population on the central Mo(V) ion (ρ_{Mo} ~ 0.8) as well as from the spin population delocalized to the ligand, ρ_L. The anisotropic *hfi* for the phosphate ligand in SO was found to be similar to the direct through-space contribution from ρ_{Mo}, whereas the 75As anisotropic *hfi* of the arsenate ligand appears to be mostly determined by the contribution from ρ_L. While it is quite possible that this qualitative difference is simply explained by the somewhat limited accuracy of the measurements and simulations, these values can be used to obtain an order-of-magnitude estimate of the anisotropic *hfi* of ^{33}S from either the ratios of the nuclear magnetic moments (μ_{33S}/μ_{31P} ~ 0.19 and μ_{33S}/μ_{75As} ~ 0.44) or the ratio of the atomic anisotropic *hfi* constants ($T_{\perp 33S}/T_{\perp 31P}$ ~ 0.57 and $T_{\perp 33S}/T_{\perp 75As}$ ~ 0.3).[15] The range of $|T_{\perp 33S}|$ values estimated in this way is from about 0.2 to 1.6 MHz.

As far as the *nqi* is concerned, we are not aware of any specific literature data for ^{33}S-enriched sulfate. However, those few data on ^{33}S *nqi* that are available for other sulfur-containing compounds[16] show that the quadrupole coupling constant, e^2Qq/h, can be as large as 50 MHz, which significantly exceeds the expected *hfi* and the ^{33}S Zeeman interaction at the magnetic fields used in our experiments (*e.g.*, at magnetic fields B_o ~ 1 T the ^{33}S Zeeman frequency, ν_I, is ~ 3.3 MHz). Since such a situation is rather exotic for systems investigated by pulsed EPR to date, we present here a simple theoretical analysis that explicitly shows the combined effect of the *hfi* and *nqi* in both the EPR and ESEEM spectra.

2. Energies and nuclear transition frequencies for I = 3/2 and strong nqi—In the case of strong *nqi*, it is convenient to consider the problem in the principal axes frame of the *nqi*, (X,Y,Z). The quadrupolar spin-Hamiltonian is:

$$H_Q = k \cdot [3I_Z^2 - I^2 + \eta(I_X^2 - I_Y^2)] \tag{1}$$

where k for $I = 3/2$ is equal to $e^2Qq/12h$ and η is the asymmetry parameter of the electric field gradient tensor on the nucleus: $0 \leq \eta \leq 1$. The energies and eigenfunctions of H_Q are:

$$E_{\pm 3/2}^Q = 3kC_\eta; \quad E_{\pm 1/2}^Q = -3kC_\eta$$
$$\psi_{\pm 3/2}^Q = c_\alpha | \pm 3/2 \rangle + s_\alpha | \mp 1/2 \rangle; \quad \psi_{\pm 1/2}^Q = c_\alpha | \pm 1/2 \rangle - s_\alpha | \mp 3/2 \rangle \tag{2}$$

where $c_\alpha = \cos\alpha$, $s_\alpha = \sin\alpha$, and $\tan 2\alpha = \eta/\sqrt{3}$. Note that the largest value of α is only 15° (reached for $\eta = 1$), and therefore $s_\alpha < 0.26$. The parameter C_η:

$$C_\eta = \sqrt{1 + \frac{\eta^2}{3}} \tag{3}$$

is introduced because it will be encountered in numerous expressions below. Since $0 \leq \eta \leq 1$, $C_\eta \approx 1$ with an accuracy of ~ 15% (for $\eta = 1$) or better.

The subscripts at the energies and wavefunctions in eq 2 show the main contributor of the original basis set to the eigenfunctions of H_Q. However, these subscripts do not reflect the average projections I_Z in the eigenstates. We will use them below in a hereditary fashion.

One can see that $\psi_{\pm 1/2}^Q$ and $\psi_{\pm 3/2}^Q$ represent two pairs of degenerate states. The energy difference between these doublet states is:

$$\Delta E^Q = 6kC_\eta = \frac{e^2Qq}{2h}C_\eta \tag{4}$$

The degeneracy is removed when the nuclear Zeeman and hyperfine interactions are present. To discuss their effect, we will consider the magnetic field vector, **B$_0$**, to have the direction cosines b_X, b_Y and b_Z with respect to the *nqi* principal axes. The spin Hamiltonian for the Zeeman and hyperfine interactions in a situation of low g-anisotropy (when the quantization axis of the electron spin coincides with **B$_0$**) is:

$$H_{ZH} = -\nu_I \cdot \sum_i I_i b_i + \sum_{i,j}(m_s b_i)A_{ij}I_j = \sum_i V_i I_i \tag{5}$$

where i and j run through X, Y and Z, ν_I is the nuclear Zeeman frequency, and A_{ij} are the components of the *hfi* tensor: $A_{ij} = a_{iso} + T_{ij}$ (a_{iso} is the isotropic *hfi* constant and T_{ij} are the components of the anisotropic *hfi* tensor) and m_s ($\pm\frac{1}{2}$) is projection of the electron spin. The V_i simply parametrize the terms that are multiplied by the same nuclear spin projection operators.

In the strong *nqi* limit, $\nu_I, A_{ij} \ll \Delta E^Q$. Then, to first approximation, only the mixing within the pairs of the degenerate states can be taken into account, and simple approximate expressions for energies and wavefunctions obtained:

$$E^{ZH}_{\pm 1/2} = -3kC_\eta \pm \sqrt{(C_\eta + 1 - \eta)^2 V_X^2 + (C_\eta + 1 + \eta)^2 V_Y^2 + (2 - C_\eta)^2 V_Z^2} / 2C_\eta$$

$$E^{ZH}_{\pm 3/2} = 3kC_\eta \pm \sqrt{(C_\eta - 1 + \eta)^2 V_X^2 + (C_\eta - 1 - \eta)^2 V_Y^2 + (2 + C_\eta)^2 V_Z^2} / 2C_\eta$$

$$\psi^{ZH}_{\pm 3/2} = c_\beta e^{\pm i\phi} \psi^Q_{\pm 3/2} \pm s_\beta \psi^Q_{\mp 3/2}; \quad \psi^{ZH}_{\pm 1/2} = c_\gamma e^{\pm i\phi} \psi^Q_{\pm 1/2} \pm s_\gamma \psi^Q_{\mp 1/2} \tag{6}$$

where $c_\beta = \cos\beta$, $s_\beta = \sin\beta$, $c_\gamma = \cos\gamma$, $s_\gamma = \sin\gamma$, and the angles β, γ, ϕ and φ are defined by:

$$\tan 2\beta = \sqrt{(C_\eta - 1 + \eta)^2 V_X^2 + (C_\eta - 1 - \eta)^2 V_Y^2} / (2 + C_\eta) V_Z$$

$$\tan 2\gamma = \sqrt{(C_\eta + 1 - \eta)^2 V_X^2 + (C_\eta + 1 + \eta)^2 V_Y^2} / (2 - C_\eta) V_Z$$

$$e^{i\varphi} = \left[(C_\eta - 1 + \eta) V_X - i(C_\eta - 1 - \eta) V_Y \right] / \sqrt{(C_\eta - 1 + \eta)^2 V_X^2 + (C_\eta - 1 - \eta)^2 V_Y^2}$$

$$e^{i\phi} = \left[(C_\eta + 1 - \eta) V_X - i(C_\eta + 1 + \eta) V_Y \right] / \sqrt{(C_\eta + 1 - \eta)^2 V_X^2 + (C_\eta + 1 + \eta)^2 V_Y^2} \tag{7}$$

The nuclear transition frequencies within the doublet states (intradoublet frequencies) are:

$$\nu_{1/2} = \sqrt{(C_\eta + 1 - \eta)^2 V_X^2 + (C_\eta + 1 + \eta)^2 V_Y^2 + (2 - C_\eta)^2 V_Z^2} / C_\eta$$

$$\nu_{3/2} = \sqrt{(C_\eta - 1 + \eta)^2 V_X^2 + (C_\eta - 1 - \eta)^2 V_Y^2 + (2 + C_\eta)^2 V_Z^2} / C_\eta \tag{8}$$

Because of parametrization, these equations are not very useful for practical estimates. However, several levels of simplification are possible. If only the A_{ii} terms are retained, these equations reduce to:

$$\nu^{1/2,3/2} = \sqrt{\left(\nu_X^{1/2,3/2} b_X\right)^2 + \left(\nu_Y^{1/2,3/2} b_Y\right)^2 + \left(\nu_Z^{1/2,3/2} b_Z\right)^2} \tag{9}$$

where:

$$\nu_X^{1/2} = (C_\eta + 1 - \eta) \cdot |\nu_I - m_s A_{XX}| / C_\eta \approx (2 - \eta) \cdot |\nu_I - m_s A_{XX}|$$

$$\nu_Y^{1/2} = (C_\eta + 1 + \eta) \cdot |\nu_I - m_s A_{YY}| / C_\eta \approx (2 + \eta) \cdot |\nu_I - m_s A_{YY}|$$

$$\nu_Z^{1/2} = (2 - C_\eta) \cdot |\nu_I - m_s A_{ZZ}| / C_\eta \approx |\nu_I - m_s A_{ZZ}|$$

$$\nu_X^{3/2} = (C_\eta - 1 + \eta) \cdot |\nu_I - m_s A_{XX}| / C_\eta \approx \eta \cdot |\nu_I - m_s A_{XX}|$$

$$\nu_Y^{3/2} = (1 + \eta - C_\eta) \cdot |\nu_I - m_s A_{YY}| / C_\eta \approx \eta \cdot |\nu_I - m_s A_{YY}|$$

$$\nu_Z^{3/2} = (2 + C_\eta) \cdot |\nu_I - m_s A_{ZZ}| / C_\eta \approx 3 \cdot |\nu_I - m_s A_{ZZ}| \tag{10}$$

are the intradoublet frequencies that will be observed for $\mathbf{B_o}//X$, Y or Z. The last (rightmost) expression in each line of eqs 10 is accurate to linear terms in η. Similar expressions for $\nu_{X,Y,Z}^{1/2,3/2}$, although in a parametrized form, were derived previously by Alonso, *et al.*[17] The explicit expressions obtained in that work were only given for an axial *nqi* tensor ($\eta = 0$).

The final simplification results from assuming that the *hfi* is dominated by the isotropic *hfi* constant, in which case all of the intradoublet frequencies have the generic form:

$$\nu^{1/2,3/2} = c_{hq} \cdot (\nu_I \pm A/2) \tag{11}$$

with $1 \leq c_{hq} \leq 2+\eta$ for $v^{1/2}$ and $\eta \leq c_{hq} \leq 3$ for $v^{3/2}$. We have intentionally written "A" instead of "a_{iso}" in eq 11 because the same expression holds also for arbitrary relative magnitudes of isotropic and anisotropic interactions if $\mathbf{B_o}$ is oriented along any of the principal axes of the *nqi* (see eqs 9 and 10). While not very accurate for a general orientation, this expression represents a convenient tool for interpreting the cross-peaks in HYSCORE spectra (see below).

The generic expressions for transition frequencies between the energy levels belonging to different doublets (interdoublet frequencies) are:

$$v_{id} = \Delta E^Q \pm \frac{v^{1/2}}{2} \pm \frac{v^{3/2}}{2} = \Delta E^Q \pm c_{hq} \cdot (v_I \pm A/2) \tag{12}$$

where the operations of addition and subtraction are independent. The last (rightmost) expression corresponds to the same approximation as eq 11, but the range of the scaling factor c_{hq} is from -2 to 2.

3. Hyperfine splittings in the EPR spectra—Handling the expressions for energies (eqs 6) in the similar way as we did for frequencies (see eqs 10), we can easily obtain the *hfi* splittings between the lines of the allowed transitions in the EPR spectra:

$$\begin{aligned}
&\tilde{A}_X^{1/2} \approx (2-\eta) \cdot A_{XX}; \quad \tilde{A}_Y^{1/2} \approx (2+\eta) \cdot A_{YY}; \quad \tilde{A}_Z^{1/2} \approx A_{ZZ} \\
&\tilde{A}_X^{3/2} \approx \eta \cdot A_{XX}; \quad\quad \tilde{A}_Y^{3/2} \approx \eta \cdot A_{YY}; \quad\quad \tilde{A}_Z^{3/2} \approx 3 \cdot A_{ZZ}
\end{aligned} \tag{13}$$

where $\tilde{A}^{1/2}$ are the splittings between the lines of $\psi_{1/2}^{ZH}(m_s=1/2) \leftrightarrow \psi_{1/2}^{ZH}(m_s=-1/2)$ and $\psi_{-1/2}^{ZH}(m_s=1/2) \leftrightarrow \psi_{-1/2}^{ZH}(m_s=-1/2)$ transitions, and $\tilde{A}^{3/2}$ are the splittings between the $\psi_{3/2}^{ZH}(m_s=1/2) \leftrightarrow \psi_{3/2}^{ZH}(m_s=-1/2)$ and $\psi_{-3/2}^{ZH}(m_s=1/2) \leftrightarrow \psi_{-3/2}^{ZH}(m_s=-1/2)$ transition lines. Only when $\mathbf{B_o}$//Z will the usual pattern of four equidistant allowed lines be observed; for other orientations, the EPR lines become non-equidistant, and, in addition, the splittings $\tilde{A}^{3/2}$ become smaller than $\tilde{A}^{1/2}$. It is obvious that since the orientation of the *nqi* tensor with respect to g-frame is not known, it is virtually impossible to obtain an accurate *hfi* estimate from the splittings observed at canonical orientations of the g-anisotropic EPR spectrum.

If the *hfi* is sufficiently weak, no resolved splittings, but rather a simple broadening of the EPR lines, will be observed. In this case, some estimates can be made from the increase of the second moment of the EPR features. For $I = 3/2$ without *nqi* the second moment due to the allowed EPR transitions is

$$M = (5/4)A^2 \tag{14}$$

It follows from eqs 13 that eq 14 is also valid for the strong *nqi* case when $\mathbf{B_o}$//Z. On the opposite end is the situation of $\mathbf{B_o}$//X(Y) and $\eta = 0$ (axial *nqi* tensor). In this case $\tilde{A}^{1/2} = 2A$, $\tilde{A}^{3/2} = 0$, and the second moment due to allowed transitions is:

$$M = (1/2)A^2 \tag{15}$$

Equations 14 and 15 give an idea about a possible error ($\sim 50\%$) in estimating the *hfi* from the EPR broadening without knowing the relative orientation of the *nqi* tensor.

4. Interpretation of the ESEEM spectra—Let us now discuss the use of the theory formulated above for interpreting the ESEEM spectra in general and HYSCORE in particular. The most useful expressions for a qualitative interpretation are those given by eqs 11 and 12. While not very accurate, they provide simple guidelines for obtaining starting estimates of the *hfi* and *nqi* parameters that can be then refined by means of numerical simulations. For example, high transition frequencies (much greater than v_I) can be attributed to the interdoublet transitions (eq 12) and can provide a crude estimate for the quadrupole coupling constant. The lower frequencies may be attributed to $v^{1/2}$ and $v^{3/2}$.

A useful observation can be made about relative amplitudes of the $v^{1/2}$ and $v^{3/2}$ harmonics. While the functions Ψ^{ZH} (eqs 6) are generally different for the electron spin manifolds with = 1/2 and −1/2, the differences between $\psi^{ZH}_{\pm 3/2}(m_s=1/2)$ and $\psi^{ZH}_{\pm 3/2}(m_s=-1/2)$ are generally smaller than those between $\psi^{ZH}_{\pm 1/2}(m_s=1/2)$ and $\psi^{ZH}_{\pm 1/2}(m_s=-1/2)$. The physical reason for this is that the $\psi^{Q}_{\pm 3/2}$ states are only mixed by the *hfi* in proportion with the contribution of $|\pm 1/2\rangle$ components (expressed by the factor s_α in eqs 2). Since such differences are responsible for the transition branching in pulsed experiments and ultimately determine the ESEEM amplitude, the amplitude for the $v^{3/2}$ harmonics is expected to be generally smaller than that for the $v^{1/2}$ ones, and in assigning the low-frequency lines our first choice should be $v^{1/2}$.

Let us consider HYSCORE spectra. In the so-called weak *hfi* regime ($v_I > A/2$) the main correlation peaks in a HYSCORE spectrum correspond to pairs of similar (*e.g.*, both 1/2 ↔ −1/2 or both 1/2 ↔ 3/2) nuclear transitions within the electron spin manifolds with $m_S = \pm 1/2$. For a pair of cross peaks at (v_1, v_2) and (v_2, v_1) the center frequency $v_c = (v_1 + v_2)/2$ is found. If v_c is within the range $v_I \leq v_c \leq 3v_I$, then, most likely, the cross-peaks should be ascribed to $v^{1/2}$ frequencies. If $v_c \leq v_I$ then the cross-peaks can be attributed to $v^{3/2}$ frequencies. If $v_c > 3v_I$, then the lines observed are those of interdoublet frequencies. If, for example, the pair of peaks is attributed to the $v^{1/2}$ frequencies, then c_{hq} is found as v_c/v_I, and the *hfi* constant is estimated by dividing the observed splitting by c_{hq}. Of course, unique assignments are not always possible. For example, $v_I \leq v_c \leq 3v_I$ can formally correspond both to $v^{1/2}$ or $v^{3/2}$, although because of expected greater amplitude, the assignment to $v^{1/2}$ is more probable. Such situations can be resolved by numerical simulations.

Results and discussion

1. CW EPR data

The X-band CW EPR spectra of ^{32}S- and ^{33}S-At-SO are presented in Figure 1. From comparison of the spectra it is evident that the ^{33}S-At-SO spectrum shows a slight line broadening due to the unresolved ^{33}S *hfi*. While for sufficiently strong *hfi* the splitting of the features at the EPR turning points into four resolved lines could be observed, our preliminary *hfi* estimates derived from comparison with phosphate and arsenate forms of SO show that the ^{33}S *hfi* constant is likely to be smaller than the characteristic linewidth of the canonical features of the EPR spectrum of ^{32}S-At-SO ($\Delta B_0 \sim 0.5$ mT, if expressed in magnetic field units, or $\Delta v \sim 15$ MHz in frequency units). The observation of broadening thus confirms that our preliminary estimates are valid, at least, to an order of magnitude.

As we have seen in the theoretical section, in the case of strong *nqi* the EPR splittings strongly depend on the rhombicity of the *nqi* tensor and on the orientations of the *hfi* and *nqi* tensors with respect to each other and to the principal axes system of the g-factor (g-frame). The principal axes of the g-frame will be denoted x, y and z (note that the capital X, Y and Z denote the principal axes of the *nqi*, see the theoretical section). In the absence of orientational information, it is difficult to quantitatively interpret the EPR broadening. Still, some qualitative estimates can be made using the method of second moments. For example, treating the features

at the EPR turning points as separate Gaussian lines, from the broadening observed at the low-field EPR turning point (g_z), we obtain:

$$\Delta M = M_{33_S} - M_{32_S} \approx \frac{\Delta B^2_{33_S} - \Delta B^2_{32_S}}{4} \approx 76 MHz^2 \tag{16}$$

Using eq 14 we can then obtain $A_z \approx 8$ MHz, while eq 15 gives $A_z \approx 12$ MHz. The estimates of the other *hfi* components from the broadening at g_x (high-field turning point) and g_y obtained in a similar fashion are: $A_x \sim 4 - 6$ MHz and $A_y \sim 7 - 11$ MHz. Assuming all of the *hfi* tensor components to be of the same sign, one can estimate $|a_{iso}| \sim 6 - 10$ MHz and the anisotropic *hfi* components $|T_{ij}| \leq 4$ MHz.

The accuracy of these estimates is rather low (not better than 50%) for several reasons, the two major ones being related to approximating the canonical features by Gaussian lines and to neglecting the contribution of the forbidden transitions to the second moments. Still, these estimates confirm the existence of an essentially non-zero ^{33}S *hfi* whose magnitude is in qualitative agreement with the preliminary estimates derived from comparison with the phosphate and arsenate ligands (see the theoretical section), and thus prove the presence of a sulfate ligand at the Mo(V) center. While this observation serves the *qualitative* purpose of this work, obtaining a more detailed information about the ^{33}S *hfi* and *nqi* parameters is certainly desirable because it may provide a key to the electronic and geometrical structure of the Mo-O-SO$_3$ fragment, and also enable meaningful comparisons with other forms of SO in which the Mo(V) center is "blocked" by coordinated sulfate. To obtain this detailed information, the ESEEM measurements have been performed (*vida infra*).

2. Choosing the operational mw frequency for ESEEM experiments

The pulsed EPR techniques used in this investigation were two-pulse (primary) ESEEM and HYSCORE. The quality of the spectra obtained by ESEEM techniques depends, in particular, on the ESEEM amplitude. It is well-known that the ESEEM amplitude is maximized when the experiments are performed at a magnetic field, B_{opt}, for which the Zeeman interaction of the nucleus of interest is approximately cancelled by the *hfi* within one of the electron spin manifolds: $\nu_I - A/2 \sim 0$.[18] This requirement works equally well for systems with or without *nqi*. The optimal mw frequency, ν_{mw}, is then found from equating the electronic Zeeman interaction to the mw quantum energy, $h\nu_{mw} = g\beta B_{opt}$. Taking into account the preliminary *hfi* estimates ($a_{iso} \sim 4 - 6$ MHz), the optimal ^{33}S Zeeman frequency satisfying the cancellation condition is calculated to be about $2 - 3$ MHz. This frequency corresponds to $B_{opt} \sim 600 - 900$ mT and $\nu_{mw} \sim 16 - 24$ GHz. Since our instrumentation does not cover the range of the mw frequencies from 18 to 26 GHz,[19] we had to choose between using the available K$_u$-band (12 – 18 GHz) or K$_a$-band (26 – 40 GHz) spectrometers for our measurements. Because the ESEEM spectra for the weak interaction case ($\nu_I > A/2$, while, of course, keeping $\nu_I - A/2$ not far from zero) are usually easier to interpret,[18] we decided to perform the experiments at $\nu_{mw} \sim 29$ GHz ($B_0 \sim 1$ T), close to the low-frequency part of the K$_a$-band. In addition, the experiments at higher mw frequencies provide the benefit of higher signal-to-noise ratios.[20]

3. Two-pulse (primary) ESEEM

The two-pulse ESE field sweep spectrum is shown in Figure 2. The primary ESEEM measurements were performed at several magnetic field positions across this spectrum. In each of these experiments only a subset of orientations of the Mo(V) center with respect to $\mathbf{B_0}$ contributes to the ESEEM, and such measurements are called orientation-selective.[21,22] As an example, Figure 3 shows the normalized primary ESEEM traces recorded for At-SO at the low-field turning point of the EPR spectrum (g_z). The ^{32}S-At-SO trace shows some oscillations

of very small amplitude, whereas the ESEEM amplitude for ^{33}S-At-SO is quite remarkable, about 20% at the beginning of the trace. ESEEM of similar amplitude was also observed at other EPR positions. The strong ESEEM is obviously caused by the ^{33}S *hfi* and *nqi* because the only difference between the two samples is in the isotopic content of the added sulfite.

The amplitude and cosine Fourier transforms (FT) of the time domain ESEEM traces of ^{33}S-At-SO acquired at the turning points of the EPR spectrum are shown in Figures 4 and 5, respectively. In addition, Figure 4 shows the spectra of ^{32}S-At-SO. One can see from comparison that the spectral lines attributable to ^{33}S heavily dominate the spectra of ^{33}S-At-SO and occupy the range from zero to about 25 MHz. Among the ^{33}S lines there is a persistent line of positive amplitude at a frequency of about 18 MHz. This frequency is more than five times greater than the ^{33}S Zeeman frequency, $v_I \sim 3.5$ MHz at the magnetic fields $B_o \sim 1050$ – 1070 mT used in these experiments. It therefore stands to reason that the ^{33}S *nqi* is much stronger than the Zeeman and hyperfine interactions, and the analysis presented in the theoretical section is applicable to a qualitative interpretation of the spectra. We will therefore proceed with such an analysis, the final proof being, as usual, provided by numerical simulations of the spectra.

Based on the considerations of the theoretical section we can attribute the 18 MHz line to the interdoublet transitions of ^{33}S (see eq 12). The fact that this line dominates the spectra and shows very little orientational dependence leads to the suggestion that it corresponds to the electron spin manifold where the ^{33}S Zeeman interaction is approximately cancelled by the *hfi* ($v_I - A/2 \sim 0$). Therefore, this frequency should be close to ΔE^Q (see eq 4), and the quadrupole coupling constant can immediately be estimated as $e^2Qq/h \sim 36$ MHz.

The low-frequency parts of the spectra at g_z and g_x are each dominated by a single line with a positive amplitude (~10 MHz and ~7.5 MHz, respectively), which we tentatively attribute to $v^{1/2}(m_S = -1/2) \approx c_{hq}(v_I + A/2)$ (assuming A to be positive, see eq 11). If the second line of the $v^{1/2}$ doublet, $v^{1/2}(m_S = 1/2) \approx c_{hq}|v_I - A/2|$, were observed, one could accurately estimate both c_{hq} and A. That this line is not observed may be taken as an indication of some sort of a distribution of the *hfi* parameters (discussed below). In such a situation, the *hfi* constant can only be estimated by assuming $1 \leq c_{hq} \leq (3$ or $v^{1/2}/v_I$, whichever is smaller). The resulting very crude estimates $0 \leq A_z \leq 13$ MHz and $0 \leq A_x \leq 8$ MHz do overlap, however, with our preliminary expectations and with the estimates made from the EPR broadening.

The spectrum obtained at g_y is much more complex and anisotropic because for this EPR turning point many orientations of the Mo(V) center contribute to the ESEEM. Since no separate lines can be confidently distinguished in the amplitude spectrum (Figure 4) and the cosine spectrum (Figure 5) is strongly distorted by the line sidelobes resulting from non-zero dead time, we did not try to obtain any *hfi* estimates from the two-pulse ESEEM data obtained at g_y.

In the case of the two-pulse ESEEM spectra, the information about the *hfi* and *nqi* parameters can also be obtained from the amplitudes of the spectral lines. This, however, requires numerical simulations to be performed. In order to simplify such simulations we have employed a technique based on obtaining and using a so-called field-integrated (FI) ESEEM spectrum that represents a FT of a weighted sum of the ESEEM traces recorded at several magnetic fields across the EPR spectrum.[23] The statistical weights are proportional to the ESE amplitudes at these magnetic fields. If certain requirements are met (see below), the FI spectrum obtained in this way approximately corresponds to a situation of complete orientational disorder with the orientational selectivity removed (that is, to a situation of an isotropic g-factor).

While the FI spectrum can be constructed for any g-anisotropic system, it is only meaningful if the following conditions are satisfied: (a) the change of the Zeeman frequency of the nucleus

of interest for the range of magnetic fields involved in obtaining the FI spectrum is much smaller than either the relevant interaction anisotropy (*hfi* or *nqi*, or both, depending on the spin system) or the spectral linewidth determined by the time duration of the ESEEM trace, whichever is greater, and (b) the g-anisotropy is relatively small so that its effect on the anisotropic *hfi* can be neglected. Both of these conditions are satisfied for the investigated system, where the Mo (V) center has a very small g-factor anisotropy ($\Delta g/g_{iso} \sim 0.025$) and the change of the ^{33}S Zeeman frequency across the EPR spectrum ($\Delta B_o \sim 20$ mT) is only about 0.07 MHz, an order of magnitude smaller than the spectral resolution of about 0.7 MHz determined by the time duration ($\Delta \tau = 1.5$ μs) of the ESEEM trace.

The merits of using an FI spectrum stem from the fact that such a spectrum approximately corresponds to the situation of an isotropic g-factor (for the Mo(V) center of SO $g_{iso} \sim 1.98$), with the orientational selectivity removed. This allows one to reduce the number of variable parameters in numerical simulation by three (specifically, the three Euler angles describing the orientation of one of the nuclear interaction tensors, *hfi* or *nqi*, with respect to the g-frame). In addition, the numerical simulations for the orientationally-nonselective situation are usually more forgiving in terms of possible inaccuracies of the *hfi* and *nqi* parameters. While this method makes a reasonable fit easier to obtain, the range of admissible variation of parameters (*i.e.*, the uncertainty in these parameters) is generally larger than in orientation-selective simulations. Therefore, our purpose in such simulations for this complex system is to establish a possible range of variation for the most sensitive parameters of the spectrum. Other examples using such an approach have been described. [23,24]

The two-pulse FI ESEEM spectrum of ^{33}S-At-SO obtained as described above is shown at the bottom of Figures 4 (amplitude) and 5 (cosine). Figures 6 through 9 compare the experimental FI spectrum (solid line) with those simulated numerically for different sets of the *hfi* and *nqi* parameters (dashed lines). The orientation of the *nqi* tensor with respect to the anisotropic *hfi* tensor, **T**, was determined by the three Euler angles, ϕ, θ and Ψ. These angles describe three consecutive rotations of a coordinate system (or a tensor): (1) by angle ϕ around axis Z, (2) by angle θ around the new axis Y, and (3) by angle Ψ around the new axis Z. The simulation parameters are shown in Tables 2 through 5, while Table 1 explains how each cell of the parameter tables is organized. A cell at a certain position in a parameter table corresponds to the panel at the same position in the corresponding Figure. Note that sometimes the amplitudes of the simulated spectra exceeded that of the experimental spectrum. Therefore, the vertical scales of the panels in Figures 6–9 are generally different to accommodate both the simulated and experimental spectra.

Figure 6 shows the results of the simulation for weak anisotropic *hfi* ($T_\perp = -0.1$ MHz) and axial *nqi* ($\eta = 0$). The central panel corresponds to the best fit (achieved at $a_{iso} \approx 4.6$ MHz and $e^2Qq/h = 40.5$ MHz), while other panels show simulations for $a_{iso} = 4.6 \pm 1.0$ MHz and $e^2Qq/h = 40.5 \pm 5.0$ MHz). One can see that the *nqi* mostly determines the position of the spectral line at 18 MHz, while the *hfi* constant mostly determines its amplitude. The simulations confirm that the 18 MHz line belongs to the interdoublet transitions of ^{33}S within the electron spin manifold where the ^{33}S Zeeman interaction is approximately cancelled by the *hfi*.

The purpose of the simulations presented in Figure 7 is to establish the effect of the anisotropic *hfi* and the orientation of the *nqi* tensor with respect to the *hfi* tensor. The simulation strategy was to set a certain anisotropic *hfi* tensor and orientation of the *nqi* tensor and then try to obtain the best possible fit by varying a_{iso} and e^2Qq/h. The *nqi* tensor was kept axial in these simulations. The main conclusion from these simulations is that an increase in the anisotropic *hfi* results in an increase of the amplitude of the $v^{1/2}$ transition lines that are observed at the frequencies below 18 MHz. Starting from $|T_{kk}| \sim 2 - 3$ MHz, any reasonable fit becomes impossible to obtain.

The simulations shown in Figure 8 were performed for a rhombic *nqi* tensor (the limiting case of $\eta = 1$), while in other respects they were similar to those shown in Figure 7. Also in this case, a qualitative agreement between the simulated and experimental spectra could be achieved. Summarizing the results of the numerical simulations, the following limits of variation of the *hfi* and *nqi* parameters were obtained: $3.4 \leq |a_{iso}| \leq 5.0$ (MHz); $|T_{kk}| < 2 - 3$ MHz; $33 \leq |e^2Qq/h| \leq 41$ (MHz). The simulations proved to be insufficiently sensitive to narrow down the possible limits for the *nqi* asymmetry parameter, η, and for the relative orientations of the *nqi* and *hfi* tensors.

Finally, Figure 9 shows the results of simulations for uncoordinated sulfate. The lack of coordination was parametrized as $a_{iso} = 0$. The Mo–S distance was assumed to be $R \approx 3.1$ Å. This distance, of course, is unrealistically short (it is about equal to that for a coordinated sulfate), but the simulation with such a small distance gives an idea about the largest possible ESEEM amplitude one could possibly observe for uncoordinated sulfate. This simulation shows that, depending on the strength of the *nqi*, either the spectral shape or amplitude, or both, are in severe disagreement with those observed in experiment, which further proves the coordination of sulfate to the Mo(V) center in the blocked form of At-SO.

4. HYSCORE spectra

While the simulations of the two-pulse ESEEM spectra resulted in estimates of the limits for the *hfi* and *nqi* parameters, they did not provide any information about the orientations of the *hfi* and *nqi* tensors with respect to the g-frame or each other. Therefore, to obtain more detailed spectroscopic information, two-dimensional (2D) HYSCORE experiments were performed. Figures 10 a, c and e show the (++) quadrants of HYSCORE spectra obtained at the turning points of the EPR spectrum. The (+−) quadrants did not show any cross-peaks exceeding the noise level. Each HYSCORE spectrum represents a sum of spectra obtained at three different time intervals between the first and second mw pulses, $\tau = 170$, 200 and 240 ns. One can see that the HYSCORE spectra reveal pairs of cross-peaks at relatively low frequencies of (3.5,10.5) MHz at g_z, (3.6,8.6) MHz to (6.5, 6.5) MHz at g_y and (2.2,7.5) MHz at g_x (the frequencies for only one of the peaks in each pair are shown). In addition, all spectra show diagonal lines at about 18 MHz and at 9.4 MHz (g_z), 7.4 MHz (g_y), and 7.0 MHz and 8.2 MHz (g_x). Regarding the diagonal features, we can mention that they can originate from the usual stimulated ESEEM due to the incomplete inversion of the electron spins by the third mw pulse. [25] While this does not change the interpretation of the 18 MHz line as belonging to one of the interdoublet transitions, we will not attempt to reproduce the diagonal lines in our HYSCORE simulations.

As mentioned in the theory section, the low-frequency lines most likely are those of $\nu^{1/2}$ transitions, with the frequencies described by eq 11. From this assignment we can obtain $c_{hq} = 1.64$ at g_z, 1.74 at g_y and 1.37 at g_x. It follows from these correction factors that if the *nqi* tensor is close to axial then its main axis should be not far from the x-axis of the g-tensor (for an exactly axial tensor an angle of about 33° can be estimated). Using the correction factors obtained and the observed splittings between the cross-peaks, the true *hfi* splittings are estimated as 4.3, 2.9 and 3.9 MHz at g_z, g_y and g_x, respectively. From these splittings, depending on their relative signs, four different sets of *hfi* constants can be estimated (see Table 6). Only set I is close to the *hfi* limits established by the simulations of the two-pulse ESEEM; for the three other sets, either the anisotropic *hfi* is too strong or the isotropic *hfi* is too weak. Therefore, set I from Table 6 is taken as the starting approximation for numerical simulations of the HYSCORE spectra, with the *nqi* axis initially oriented along g_x. In the simulations, all of the parameters were varied. A reasonable agreement between the experimental and simulated HYSCORE spectra was obtained for $a_{iso} = 3.3$ MHz and the anisotropic *hfi* tensor in the principal axes system $(T_{11}, T_{22}, T_{33}) = (1.3, 1.5, -2.8)$ MHz. The quadrupole coupling constant

$e2Qq/h = 40$ Hz agreed with the estimates made from the two-pulse ESEEM spectra, and the asymmetry parameter was found to be close to zero, $\eta < 0.3$ (near-axial *nqi* tensor). The orientations of the *hfi* and *nqi* tensors relative to the g-frame were described by the sets of Euler angles $(\phi_h, \theta_h, \Psi_h) = (90°, 90°, 0°)$ and $(\phi_q, \theta_q, \Psi_q) = (0°, 75°, 0°)$, respectively. The simulated HYSCORE spectra are shown in Figures 10 b, d and f.

The *hfi* parameters estimated from HYSCORE are slightly outside the limits predicted by the two-pulse ESEEM simulations. In addition, trial two-pulse simulations for these parameters resulted in similar ESEEM amplitude, but the agreement in the line positions was very approximate. A possible reason for these problems is that the simulations were performed for a fixed set of parameters, even though the parameters are actually likely to be statistically distributed within some limits, as has been generally observed for the Mo(V) centers of sulfite oxidizing enzymes.[7] However, the fact that the parameters estimated from two-pulse ESEEM are in reasonable agreement with those obtained from HYSCORE indicates that the distribution limits for the *hfi* are probably not large, and consequently, the HYSCORE parameters reflect the most probable statistical realization.

The idea of distributed *hfi* parameters is supported by the fact that the *hfi* parameters of the exchangeable ligands in SO are always distributed in some limits.[8] The difficulty with simulating distributed spectra, apart from the dramatic increase of the simulation time, lies in the fact that the distributions for different parameters are expected to be correlated (*e.g.*, a change of orientation of the ligand will produce simultaneous correlated changes in the orientations of the *hfi* and *nqi* tensors with respect to the g-frame and to each other, and also a change in the magnitude of a_{iso}), and evidence for such a correlation should be obtained from an independent source or model. Therefore, we have not yet attempted to perform the distributed simulations.

5. The discussion of the hfi parameters

Let us discuss the electronic-structural aspects of the *hfi* parameters obtained. Since the absolute sign of the *hfi* constant is not known both options will be discussed. Let us first assume $a_{iso} > 0$. The atomic isotropic *hfi* constant for the unpaired electron on a 3*s* orbital of ^{33}S is about 3465 MHz.[15] Therefore, $a_{iso} \sim 3$ MHz would indicate a spin population of about 0.3% for the sp^3 – hybrid orbital of sulfur in sulfate. With the atomic anisotropic *hfi* constant for the 3*p* orbital of $T_{\perp 3p} \sim -100$ MHz,[15] such a spin density will give $T_{\perp OS} \sim -0.23$ MHz. The Mo-S distance is ~ 3.1 Å, and the $T_{\perp Mo} \sim -0.15$ MHz (for the spin population of Mo(V) $\rho_{Mo} \sim 85\%$). Finally, a typical figure for the spin population on the ligand oxygen is $\rho_O \sim 5\%$.[26] The contribution of this spin population to the ^{33}S anisotropic *hfi* is $T_{\perp O} \sim -0.09$ MHz ($R_{OS} \sim 1.45$ Å). Even if all of the contributions to the anisotropic *hfi* tensor were lined up (which is not the case because the electronic orbitals of the oxygen of the Mo-O-S fragment are, probably, close to sp^3 hybrids), the total anisotropic *hfi* constant would be $T_{\perp max} \sim -0.5$ MHz, which is far smaller than the anisotopic *hfi* evaluated from simulations of the experimental spectra and of the wrong sign relative to a_{iso}.

The opposite situation of a negative a_{iso} could take place if the O-S bond were nearly perpendicular to the equatorial plane of the complex (the relevant model analogy here is the case of a β-proton in aromatic hydrocarbon radicals). Since the spin polarization constants for the Mo-O-S system in general and the O-S fragment in particular are not known, the magnitude of a_{iso} is difficult to predict from qualitative considerations. However, from comparison with other systems of heteroatoms (C, N, O)[22] values on the order of -1 to -2 MHz seem reasonable. The spin population of the sulfur orbital participating in the O-S bond in this case is again very small, ~ -0.2%, and cannot explain a relatively strong anisotropic *hfi* constant.

From the above considerations it appears that the only way to obtain the relatively strong anisotropic *hfi* of ^{33}S is to delocalize about 1.5 % of spin population to two or three of its hybrid orbitals. Such a spin delocalization is plausible because the hybrid orbitals of sulfur and of the oxygen atom directly coordinated to Mo can overlap (although less efficiently than pure π-orbitals) thus creating a π-system spanning the Mo-O-S fragment. Let us consider two sulfur orbitals, each bearing a spin population of 1.5%. If these orbitals were of pure p-type, the total anisotropic *hfi* tensor produced by them would be **T** ~ (1.5, 1.5, −3) MHz, with the main axis oriented perpendicular to the plane formed by these two orbitals. The isotropic *hfi* constant will be induced by the spin polarization of the *s*-orbital by the unpaired electron on the *p*-orbitals. The contributions to the polarization from the *p*-orbitals will be approximately additive and of the same order of magnitude as the anisotropic *hfi* constants. Therefore, the total a_{iso} in this case is expected to be approximately 3 MHz.

While the magnitudes and relative signs of the isotropic and anisotropic *hfi* parameters predicted by such a model are in a qualitative agreement with experiment, the model itself is far from perfect because the sulfur valence orbitals in sulfate are close to sp^3 hybrids. Similar calculation for such hybrid orbitals will result in the anisotropic *hfi* still in qualitative agreement with the experiment, but in the isotropic *hfi* constant a_{iso} ~ 25 MHz. Certainly, taking into account a possible negative contribution to a_{iso} from the spin density in the lone pair oxygen orbitals (that can π-overlap with the d_{xy} orbital of Mo(V)) and the contribution to the anisotropic *hfi* from the spin density on molybdenum and oxygen will permit some *s*-character to the sulfur orbitals, but it will be much smaller than 1/4, which is the *s*-character of the sp^3 orbitals (for a similar situation with an H_2O ligand, see[27]).

The discussion above shows the difficulties of explaining the *hfi* parameters of the sulfur of the sulfate ligand, in particular, in the attempts to reconcile the relatively small isotropic *hfi* constant with the relatively strong anisotropic *hfi*. This demonstrates that the level of qualitative understanding of the spin polarization mechanisms for sulfur (in contrast with the second row elements, *e.g*., C, N, O, which were investigated in detail by quantum chemical methods[28]) is insufficient to allow reliable conclusions about the electronic and geometrical structure of the Mo-OSO$_3$ fragment to be made from the ^{33}S *hfi* parameters. Clearly, to obtain such structural information, quantum chemical (*e.g*., DFT) calculations are necessary. These calculations will be the subject of future work.

Conclusion

The first step of the generally accepted mechanism for SOs involves generation of a coordinated sulfate group from the reaction of sulfite with a terminal oxo group of the dioxomolybdenum (VI) center.[4–6] Experimentally, however, sulfate coordination in SO has never been directly observed, although we have argued in our previous work that the so-called "blocked" form of At-SO presents exactly this situation.[11] In the present work we have used CW EPR and ESEEM spectroscopic techniques to study the blocked form of At-SO prepared with ^{33}S-enriched sulfite, and have unequivocally demonstrated, for the first time, that the Mo(V) center in this form does indeed retain the sulfate ligand. This conclusion is based on findings that *hfi* constant of ^{33}S is rather large and is comparable (after scaling in proportion with the ratio of magnetic moments) with those of ^{31}P and ^{75}As in the phosphate and arsenate forms of SO.

The determination of the ^{33}S *hfi* constant was facilitated by the theoretical analysis of the nuclear transition frequencies for the system of $I = 3/2$ with strong *nqi* (as compared to the Zeeman and hyperfine interactions). The simple expressions derived in this work for the frequencies provided a transparent interpretation of the ^{33}S HYSCORE spectra and allowed us to easily estimate the *hfi* parameters.

The direct observation of the coordinated sulfate is of general importance for understanding the catalytic cycles of all sulfite-oxidizing enzymes. In addition, our preliminary results indicate that certain mutant forms of SO whose Mo(V) EPR spectra show no nearby exchangeable protons, such as *lpH* human Y343F[29] and R160Q,[30] also contain "trapped" coordinated sulfate. The detailed investigation of these varieties of SO is presently under way.

Finally, this study is only the second example of pulsed EPR detection of a ^{33}S - metal ion interaction in metalloenzymes.[31,32] These works demonstrate that with appropriate instrumentation and suitable choice of the mw frequency, the detection of ^{33}S is no more complicated than that of other biologically important quadrupolar nuclei (^{2}H, ^{14}N, ^{17}O).[33,34] This finding substantially increases the range of potential applications of pulsed EPR to biological problems.

Acknowledgements

References

1. Kisker C, Schindelin H, Pacheco A, Wehbi W, Garrett RM, Rajagopalan KV, Enemark JH, Rees DC. Cell 1997;91:973–983. [PubMed: 9428520]

2. Schrader N, Fischer K, Theis K, Mendel RR, Schwarz G, Kisker C. Structure 2003;11:1251–1263. [PubMed: 14527393]

3. Kappler U, Bailey S. J Biol Chem 2005;280:24999–25007. [PubMed: 15863498]

4. Hille R. Biochim Biophys Acta-Bioenerg 1994;1184:143–169.

5. Brody MS, Hille R. Biochim Biophys Acta 1995;1253:133–135. [PubMed: 8519792]

6. Hille R. Chem Rev 1996;96:2757–2816. [PubMed: 11848841]

7. Enemark JH, Astashkin AV, Raitsimring AM. Dalton Trans 2006:3501–3514. [PubMed: 16855750]

8. Pacheco A, Basu P, Borbat P, Raitsimring AM, Enemark JH. Inorg Chem 1996;35:7001–7008. [PubMed: 11666879]

9. George GN, Garrett RM, Graf T, Prince RC, Rajagopalan KV. J Am Chem Soc 1998;120:4522–4523.

10. Codd R, Astashkin AV, Pacheco A, Raitsimring AM, Enemark JH. J Biol Inorg Chem 2002;7:338–350. [PubMed: 11935358]

11. Astashkin AV, Hood BL, Feng CJ, Hille R, Mendel RR, Raitsimring AM, Enemark JH. Biochemistry 2005;44:13274–13281. [PubMed: 16201753]

12. Davydov RM, Yoshida T, Ikeda-Saito M, Hoffman BM. J Am Chem Soc 1999;121:10656–10657.

13. Eilers T, Schwarz G, Brinkmann H, Witt C, Richter T, Nieder J, Koch B, Hille R, Hansch R, Mendel RR. J Biol Chem 2001;276:46989–46994. [PubMed: 11598126]

14. Astashkin AV, Enemark JH, Raitsimring A. Concepts Magn Reson Part B (Magn Reson Engineering) 2006;29B:125–136.

15. Morton JR, Preston KF. J Magn Reson 1978;30:577–582.

16. Bailey WC, Gonzalez FM, Castiglione J. Chem Phys 2000;260:327–335.

17. Alonso PJ, Antorrena G, Martinez JI, Novoa JJ, Palacio F, Rawson JM, Smith JNB. Applied Magnetic Resonance 2001;20:231–247.

18. Dikanov, SA.; Tsvetkov, YuD. Electron Spin Echo Envelope Modulation (ESEEM) Spectroscopy. CRC Press; Boca Raton, Florida: 1992.

19. See: http://quiz2.chem.arizona.edu/epr/ for available pulsed EPR instrumentation and techniques.

20. Davoust CE, Doan PE, Hoffman BM. J Magn Reson 1996;A119:38–44.

21. Hoffman BM, Martinsen J, Venters RA. J Magn Reson 1984;59:110–123.

22. Hurst GC, Henderson TA, Kreilick RW. J Am Chem Soc 1985;107:7294–7299.

23. Astashkin AV, Klein EL, Enemark JH. J Inorg Biochem. 200710.1016/j.jinorgbio.2007.05.015in press

24. Raitsimring AM, Kappler U, Feng CJ, Astashkin AV, Enemark JH. Inorg Chem 2005;44:7283–7285. [PubMed: 16212344]

25. Astashkin AV, Raitsimring AM. J Magn Reson 2001;148:379–387. [PubMed: 11237645]

26. Astashkin AV, Neese F, Raitsimring AM, Cooney JJA, Bultman E, Enemark JH. J Am Chem Soc 2005;127:16713–16722. [PubMed: 16305262]

27. Getz D, Silver BL. J Chem Phys 1974;61:630–637.

28. Zhidomirov, GM.; Schastnev, PV.; Chuvylkin, ND. Quantum Chemical Calculations of Magnetic Resonance Parameters: Free Radicals. Nauka, Novosibirsk; USSR: 1978.

29. Raitsimring AM, Astashkin AV, Feng C, Wilson HL, Rajagopalan KV, Enemark JH. Inorg Chim Acta. 200710.1016/j.ica.2007.05.023in press

30. Enemark JH, Astashkin AV, Raitsimring AM, Johnson-Winters K, Klein KL, Byrne RS, Hille R, Wilson HL, Rajagopalan KV. J Biol Inorg Chem 2007;12(Suppl 1):S63.

31. Finazzo C, Harmer J, Bauer C, Jaun B, Duin EC, Mahlert F, Goenrich M, Thauer RK, Van Doorslaer S, Schweiger A. J Am Chem Soc 2003;125:4988–4989. [PubMed: 12708843]

32. Harmer J, Finazzo C, Piskorski R, Bauer C, Jaun B, Duin EC, Goenrich M, Thauer RK, Van Doorslaer S, Schweiger A. J Am Chem Soc 2005;127:17744–17755. [PubMed: 16351103]

33. Hoffman BM. Acc Chem Res 2003;36:522–529. [PubMed: 12859213]

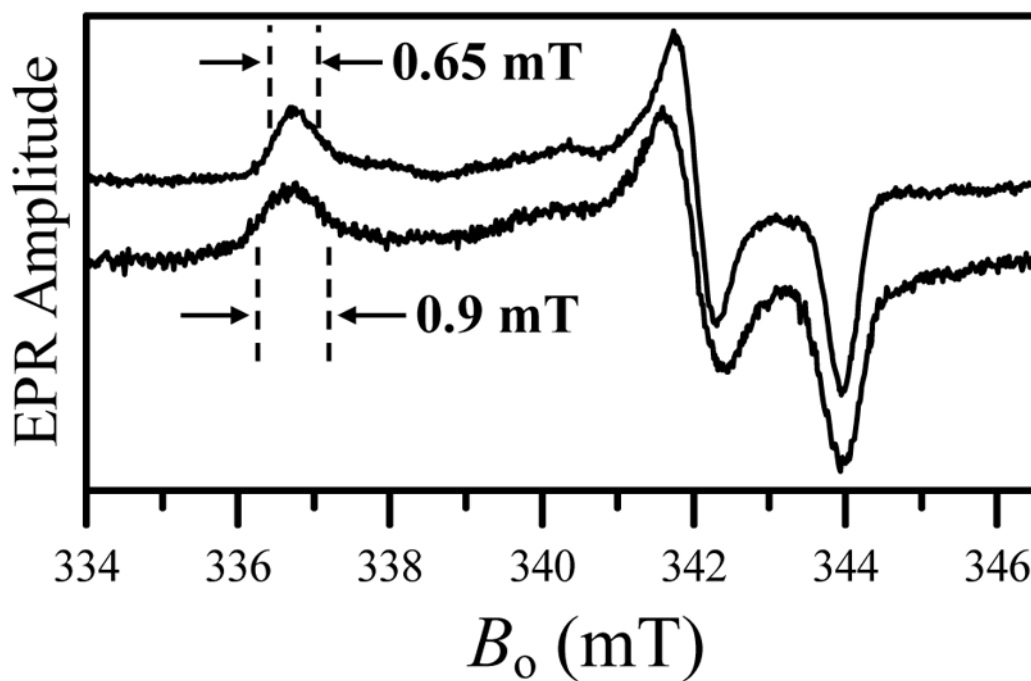34. Astashkin AV, Feng CJ, Raitsimring AM, Enemark JH. J Am Chem Soc 2005;127:502–503. [PubMed: 15643856]

Figure 1.
CW EPR spectra of *lpH* [32]S-At-SO, top, and [33]S-At-SO, bottom. Experimental conditions: v_{mw} = 9.455 GHz; mw power, 200 µW; modulation amplitude, 0.1 mT; temperature, 77K. The half-height linewidths at g_z turning point are indicated.
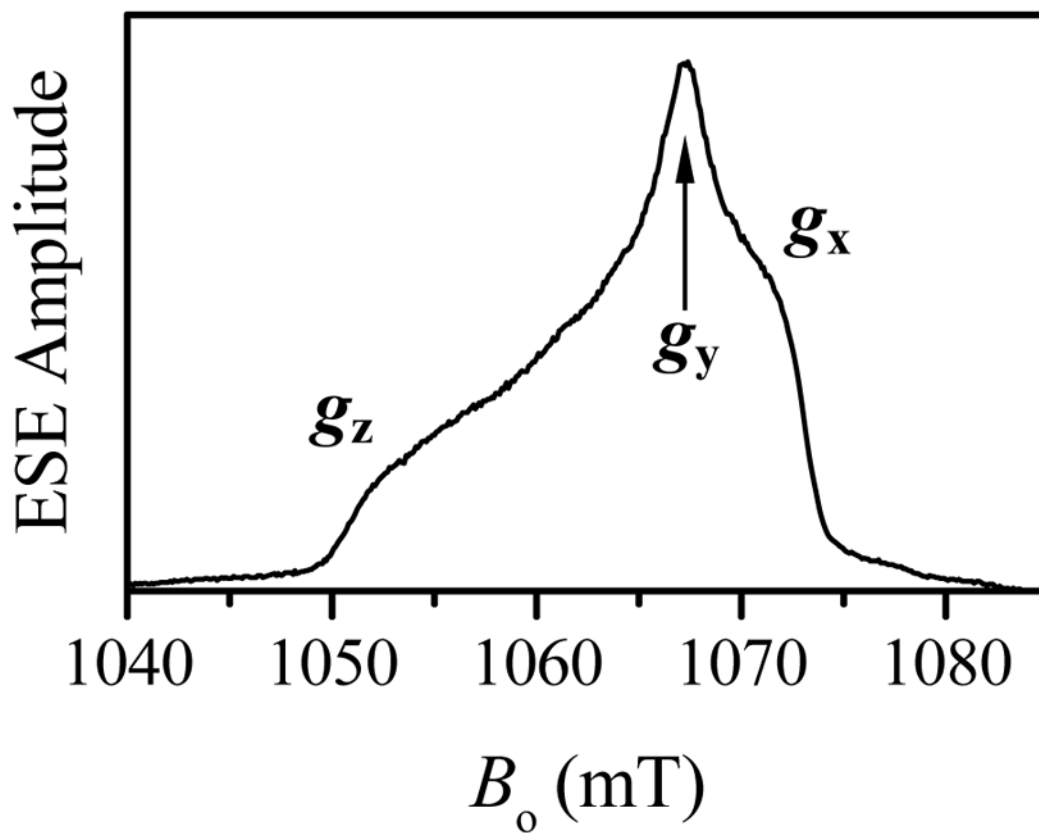
Figure 2.
Two-pulse ESE field-sweep spectrum. Experimental conditions: v_{mw} = 29.458 GHz; time interval between the mw pulses, t = 250 ns; mw pulses, 2×13 ns; temperature, 20 K.
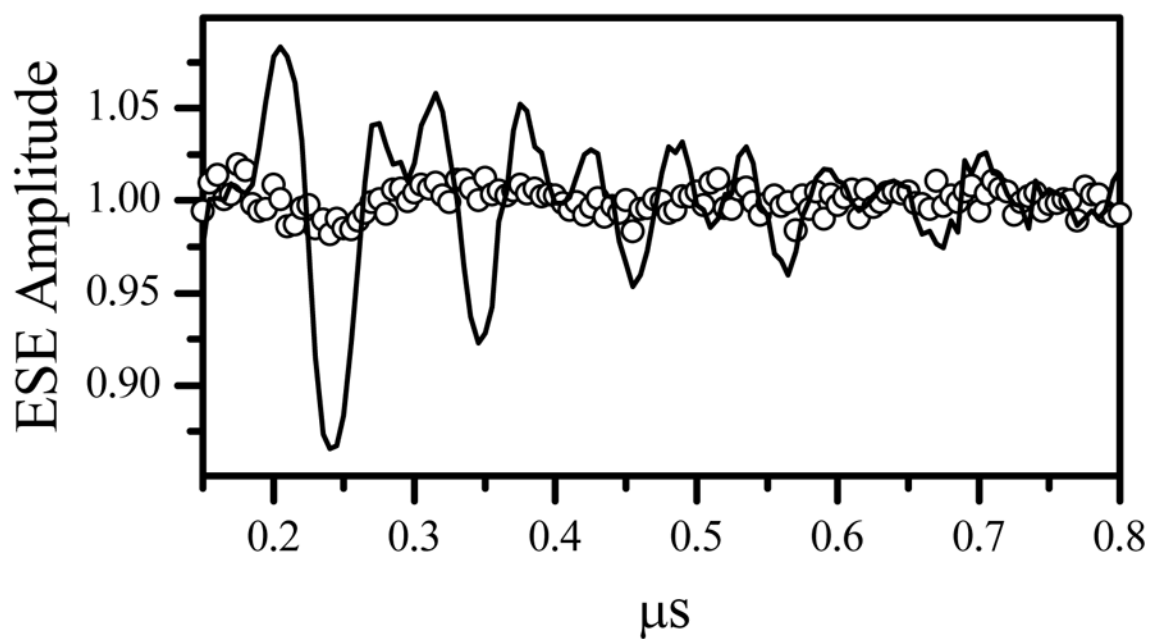
Figure 3.
Open circles and the solid line show, respectively, the normalized primary ESEEM kinetics of ^{32}S-At-SO and ^{33}S-At-SO recorded at g_z. Experimental conditions: ν_{mw} = 29.458 GHz; magnetic field, 1052 mT; mw pulses, 2×13 ns; temperature, 20 K.
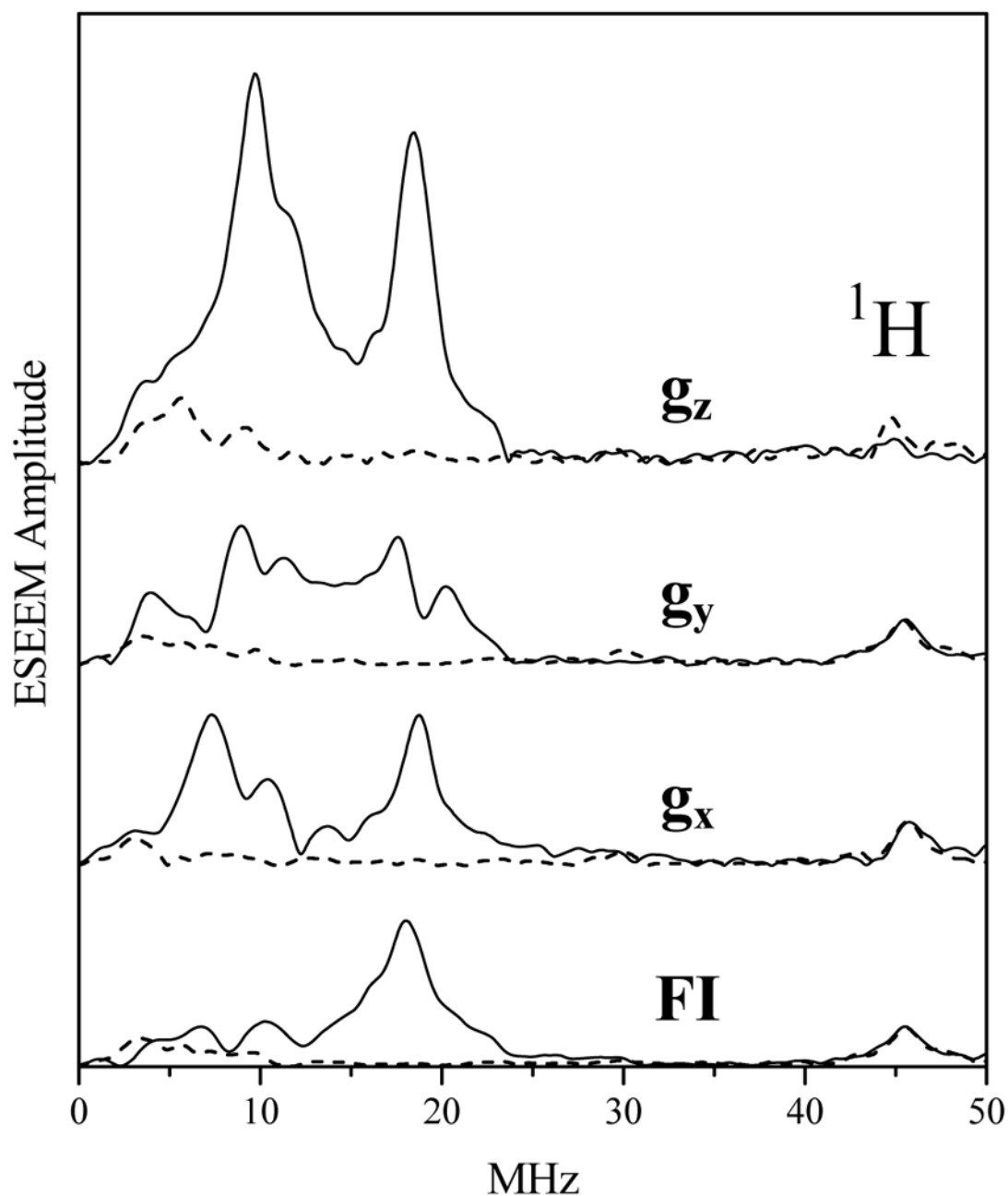
Figure 4.
Amplitude FTs of two-pulse ESEEM traces recorded for *lpH* ^{33}S-At-SO (solid traces) and ^{32}S-At-SO (dashed traces) at the EPR turning points, as indicated by the labels "g_x", "g_y" and "g_z". The bottom trace is the amplitude spectrum of the two-pulse FI ESEEM. Experimental conditions: ν_{mw} = 29.458 GHz; mw pulses, 2×13 ns; time interval between the pulses, τ = 250 ns; temperature, 20 K. The magnetic fields at g_z, g_y and g_x where the measurements were performed were, respectively, 1052 mT, 1067.2 mT and 1072.1 mT.
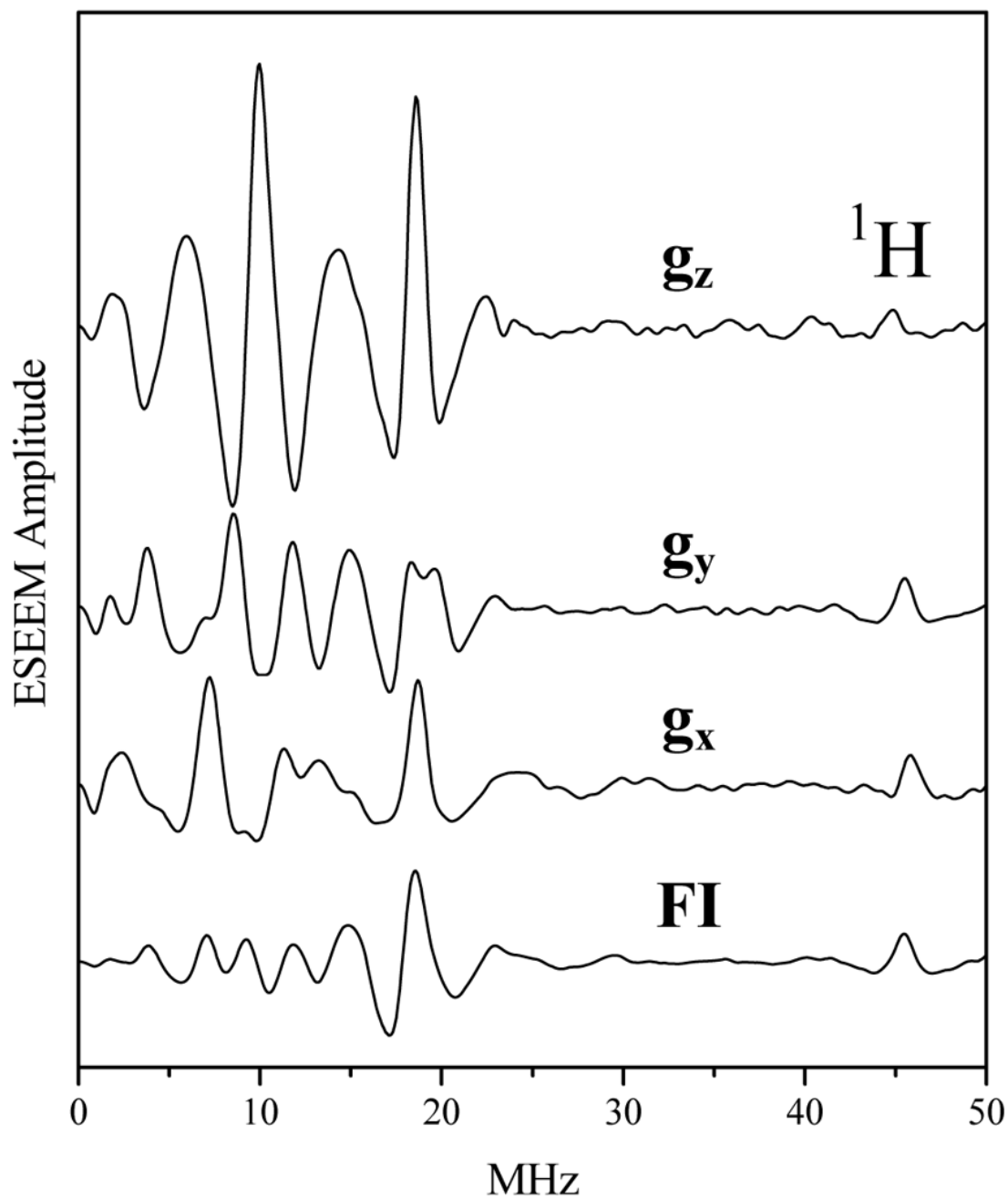
Figure 5.
Cosine FTs of two-pulse ESEEM traces recorded for *lpH* ^{33}S-At-SO at the EPR turning points, as indicated by the labels "g_x", "g_y" and "g_z". The bottom trace is the cosine spectrum of the two-pulse FI ESEEM. Experimental conditions, same as in Figure 4.
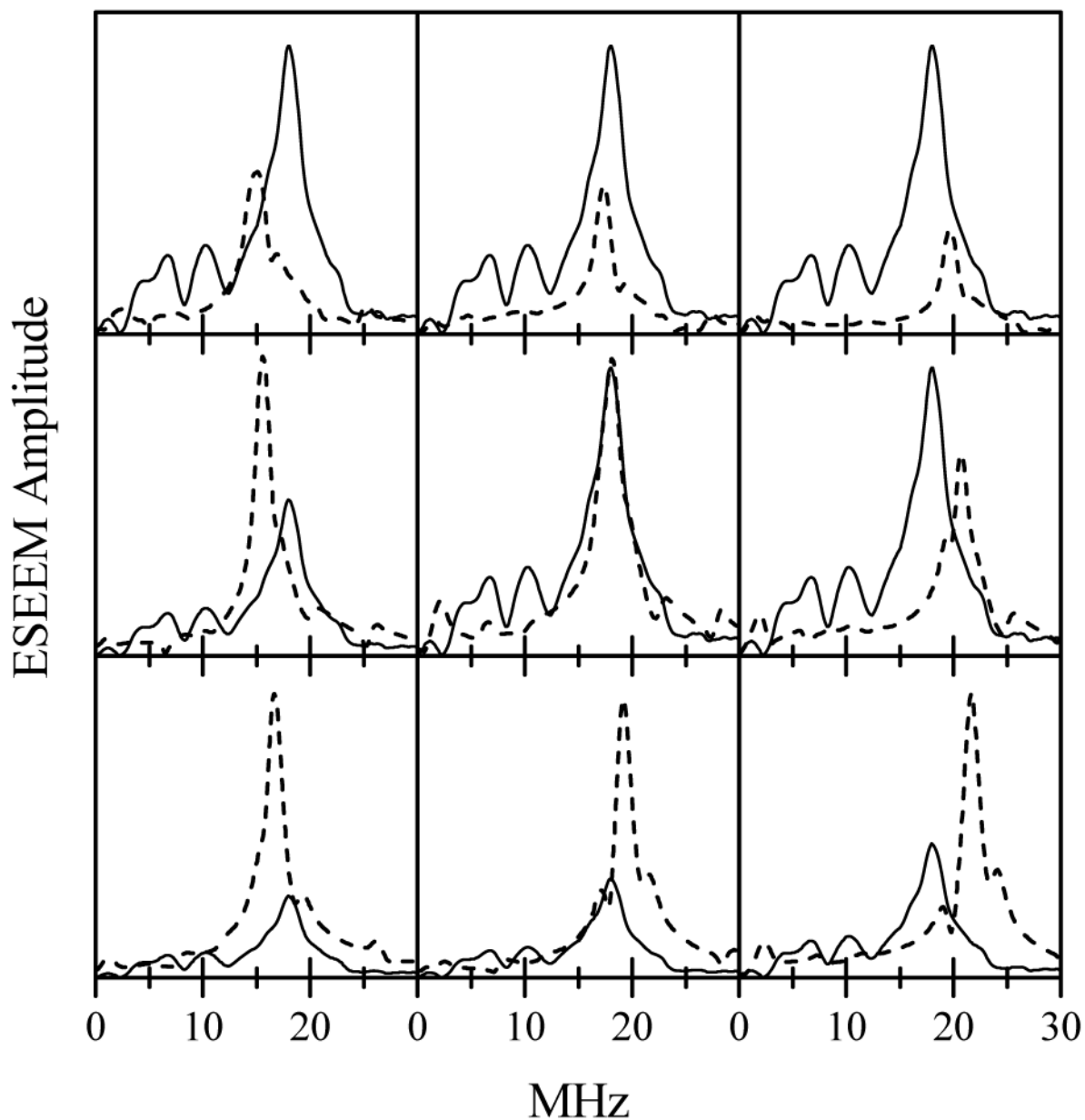
Figure 6.
Solid trace in each panel is the amplitude FT of the two-pulse FI ESEEM reproduced from
Figure 4. Dashed trace in each panel is the result of numerical simulations with the *hfi* and
nqi parameters shown in Table 2. The positions of the cells in Table 2 correspond to positions
of the panels in the Figure. The vertical scales of the panels in the Figure are generally different
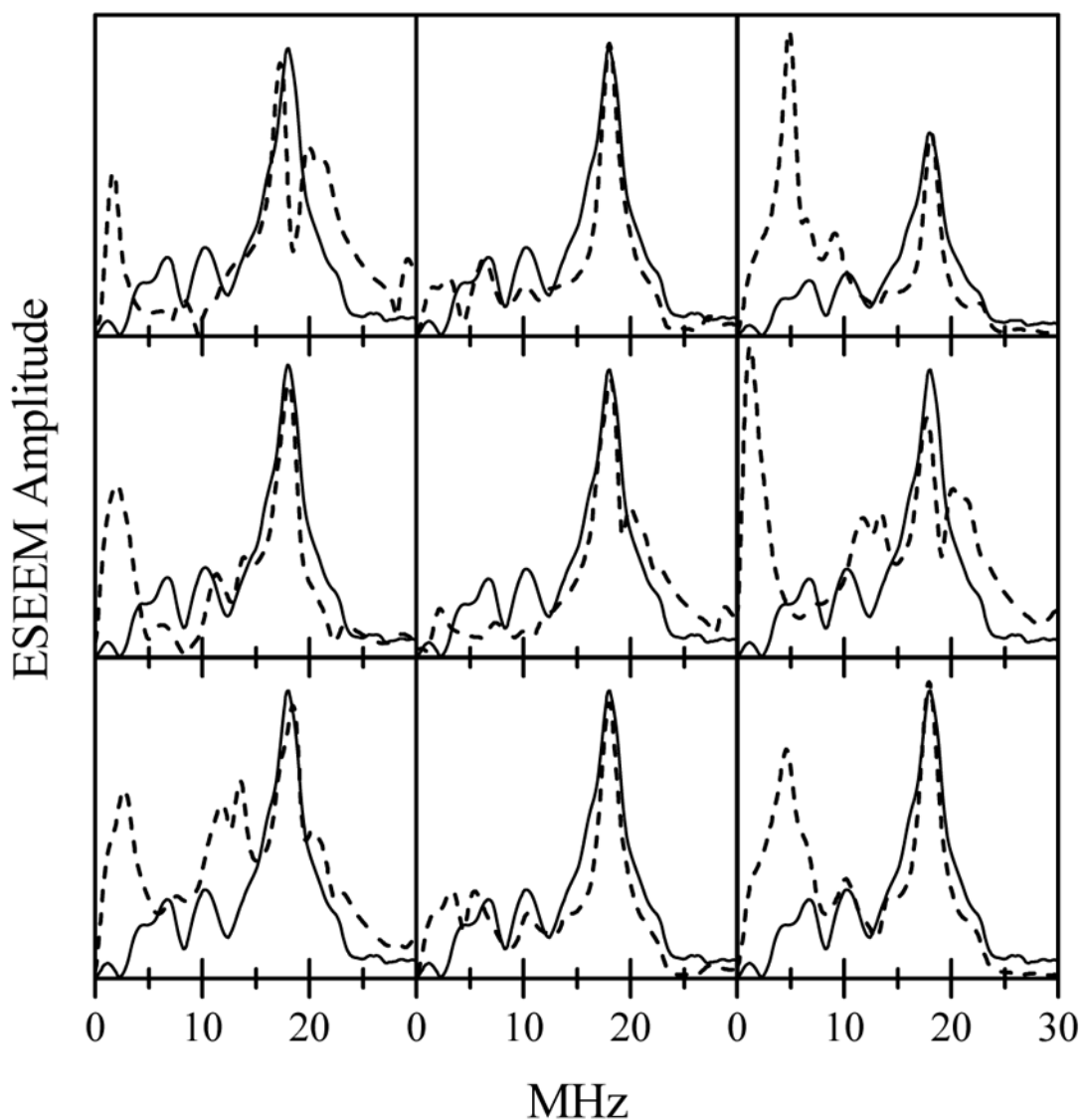to accommodate both the simulated and experimental spectra.

Figure 7.
Solid trace in each panel is the amplitude FT of the two-pulse FI ESEEM reproduced from
Figure 4. Dashed trace in each panel is the result of numerical simulations with the *hfi* and
nqi parameters shown in Table 3. The positions of the cells in Table 3 correspond to positions
of the panels in the Figure. The vertical scales of the panels in the Figure are generally different
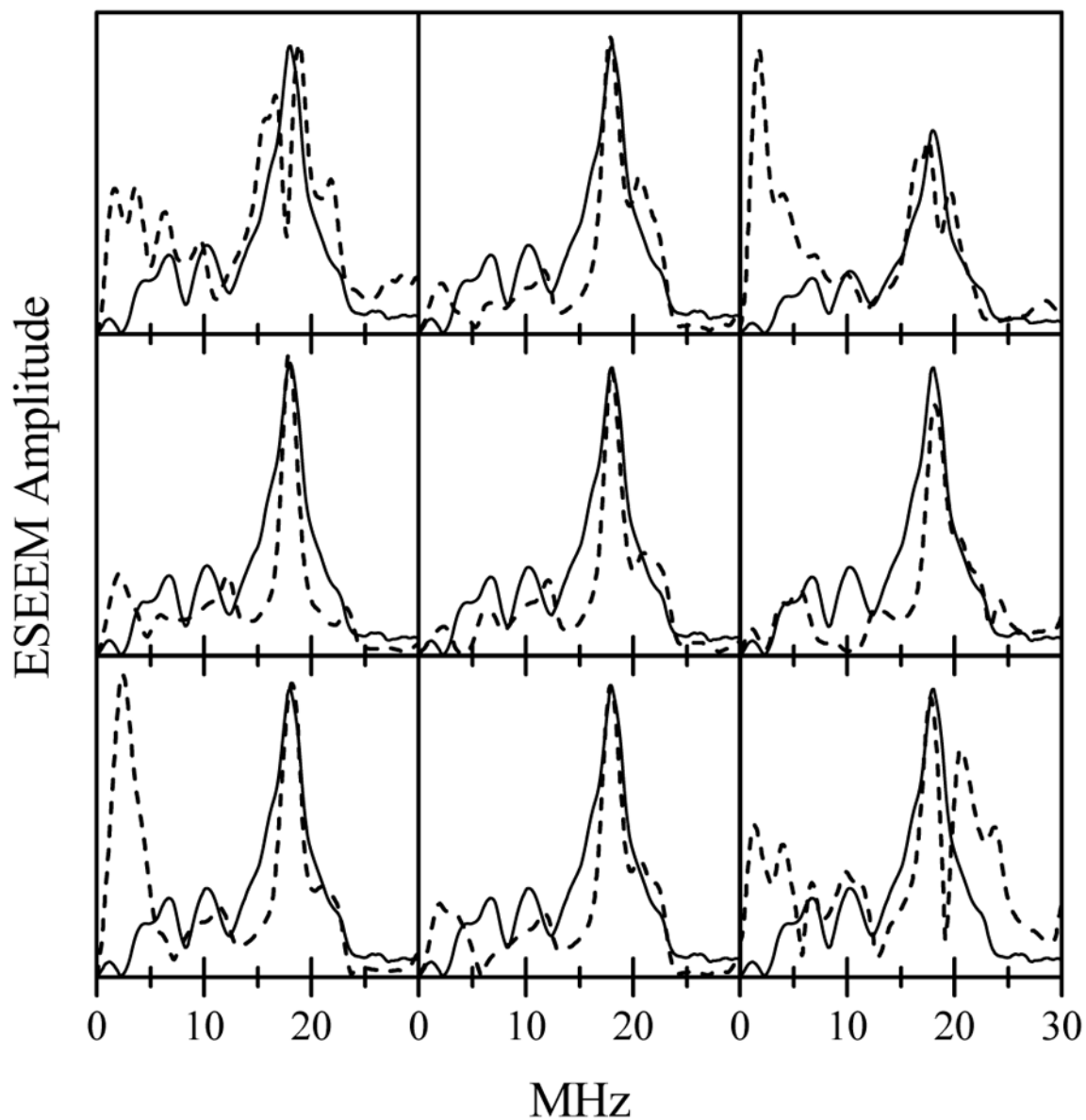to accommodate both the simulated and experimental spectra.

Figure 8.
Solid trace in each panel is the amplitude FT of the two-pulse FI ESEEM reproduced from
Figure 4. Dashed trace in each panel is the result of numerical simulations with the *hfi* and
nqi parameters shown in Table 4. The positions of the cells in Table 4 correspond to positions
of the panels in the Figure. The vertical scales of the panels in the Figure are generally different
to accommodate both the simulated and experimental spectra.

Figure 9.
Solid trace in each panel is the amplitude FT of the two-pulse FI ESEEM reproduced from Figure 4. Dashed trace in each panel is the result of numerical simulations with the *hfi* and *nqi* parameters shown in Table 5. The positions of the cells in Table 5 correspond to positions of the panels in the Figure. The vertical scales of the panels in the Figure are generally different to accommodate both the simulated and experimental spectra.
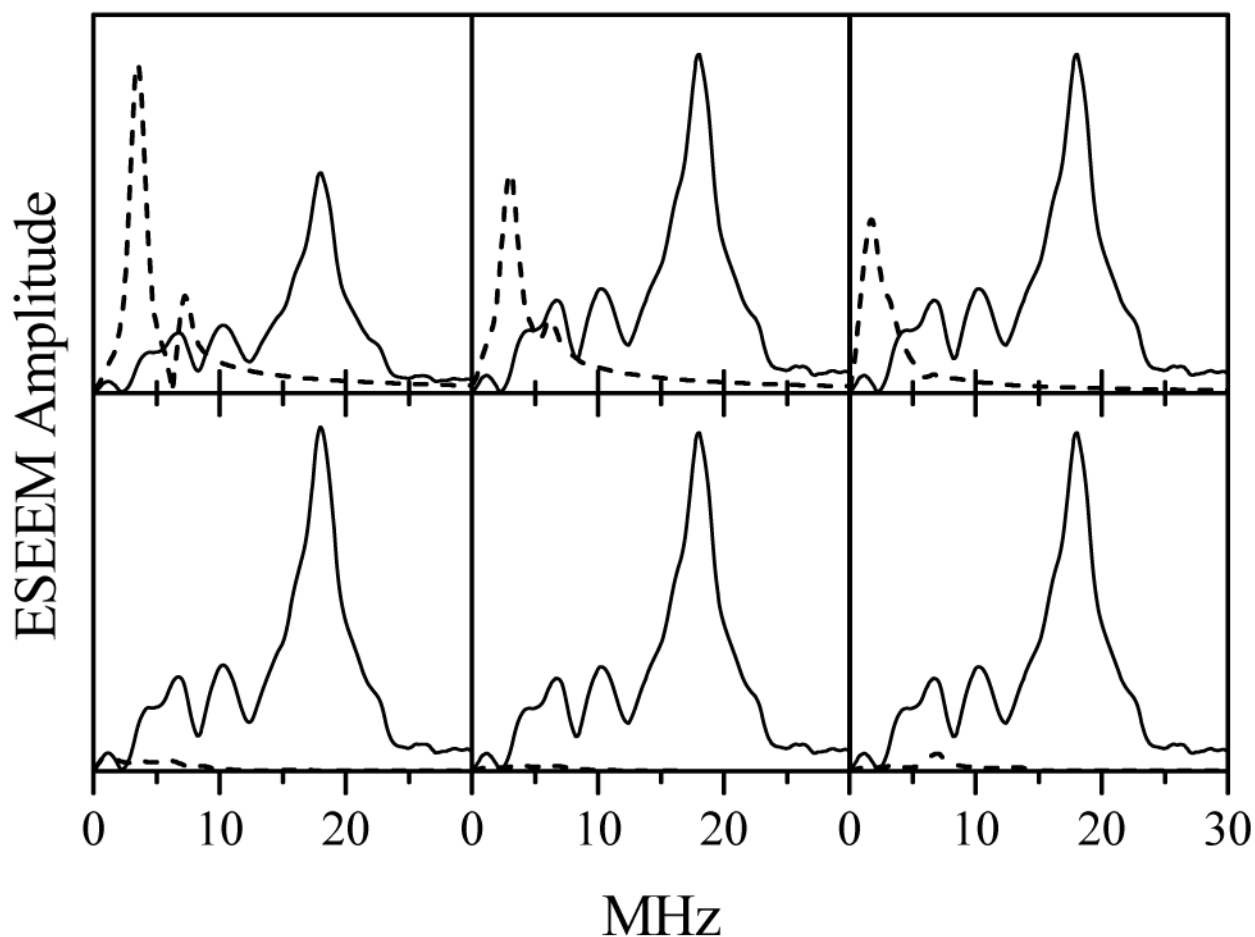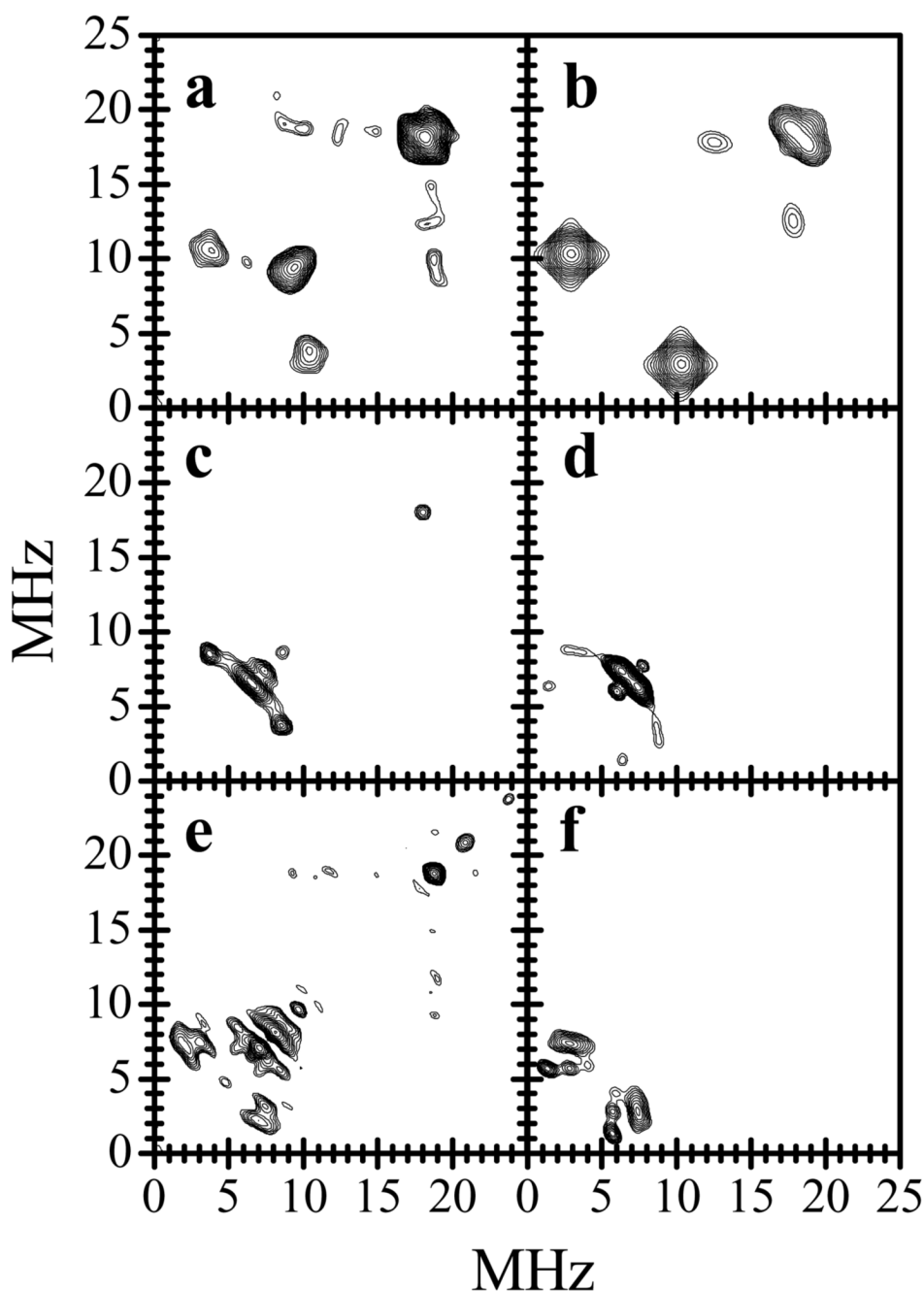
Figure 10.
Panels a, c and e, the (++) quadrants of the HYSCORE spectra of *lpH* ^{33}S-At-SO obtained at the g_z, g_y and g_x EPR turning points, respectively (B_o = 1052 mT, 1067.2 mT and 1072.1 mT, respectively). The spectra shown represent sums of the spectra obtained at time intervals between the first and second mw pulses τ = 170, 200 and 240 ns. Other experimental conditions: ν_{mw} = 29.458 GHz; mw pulses, 12, 12, 22 and 12 ns; temperature, 20 K. Panels b, d and f, simulated HYSCORE spectra for g_z, g_y and g_x at the EPR turning points, respectively. Simulation parameters: a_{iso} = 3.3 MHz, anisotropic *hfi* tensor in the principal axes system, (T_{11}, T_{22}, T_{33}) = (1.3, 1.5, −2.8) MHz; e^2Qq/h = 40 MHz; η = 0; Euler angles for the orientation of the *hfi* tensor in the g-frame: ϕ_h = 90°, θ_h = 90°, Ψ_h = 0°; Euler angles for the orientation of

the *nqi* tensor with respect to the g-frame: $\phi_q = 0°$, $\theta_q = 75°$, $\Psi_q = 0°$. The simulated spectra (as experimental ones) represent sums of the spectra calculated for $\tau = 170$, 200 and 240 ns.
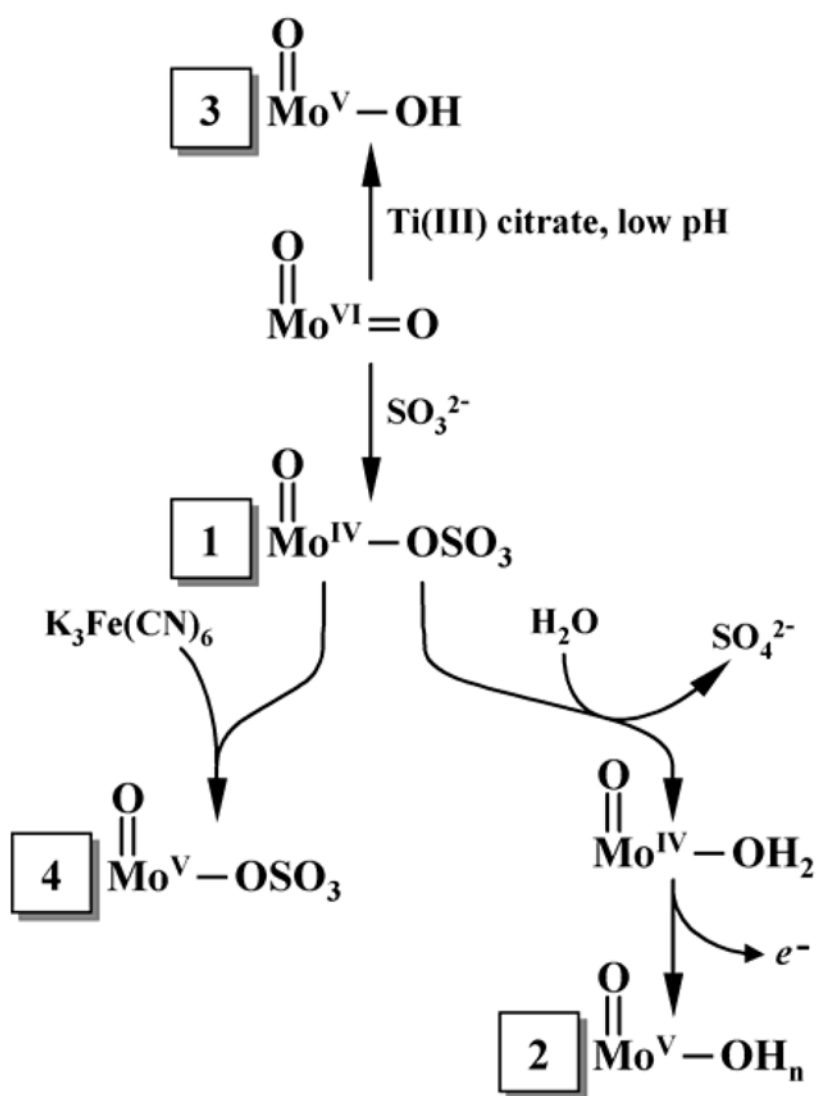
Scheme 1.

Proposed reactions for the formation of the Mo(V) forms of At-SO observed by EPR.[11] Species 4, which is formed at low pH by sulfite reduction and ferricyanide oxidation, shows no exchangeable protons and is the subject of this study using [33]S labeling.

Table 1

Explanation of the numerical values given in Tables 2 through 5. Each cell of these tables contains the spectroscopic and structural parameters in the following order (note that $T_{33} = -(T_{11}+T_{22})$):

a_{iso} [MHz]
(T_{11}, T_{22}) [MHz]
$(e^2Qq/h$ [MHz], $\eta)$
(θ, ϕ, Ψ)

Table 2

The simulation parameters for Figure 6 (seeTable 1 for explanation).

3.6 (−0.1, −0.1) (35.5, 0) (0°, 0°, 0°)	3.6 (−0.1, −0.1) (40.5, 0) (0°, 0°, 0°)	3.6 (−0.1, −0.1) (45.5, 0) (0°, 0°, 0°)
4.6 (−0.1, −0.1) (35.5, 0) (0°, 0°, 0°)	4.6 (−0.1, −0.1) (40.5, 0) (0°, 0°, 0°)	4.6 (−0.1, −0.1) (45.5, 0) (0°, 0°, 0°)
5.6 (−0.1, −0.1) (35.5, 0) (0°, 0°, 0°)	5.6 (−0.1, −0.1) (40.5, 0) (0°, 0°, 0°)	5.6 (−0.1, −0.1) (45.5, 0) (0°, 0°, 0°)

Table 3

The simulation parameters for Figure 7 (see Table 1 for explanation).

4.8	4.0	3.6
(0.5, 0.5)	(−0.5, −0.5)	(−1, −1)
(40.5, 0)	(40.5, 0)	(40.5, 0)
(0°, 0°, 0°)	(0°, 0°, 0°)	(0°, 0°, 0°)
4.5	4.9	5.0
(0.5, 0.5)	(−0.1, −0.1)	(−0.5, −0.5)
(35.5, 0)	(40.5, 0)	(45.5, 0)
(90°, 0°, 0°)	(90°, 0°, 0°)	(90°, 0°, 0°)
5.0	4.0	3.9
(−1, 0)	(−1, 0)	(−1.5, 0)
(41, 0)	(40.5, 0)	(40, 0)
(90°, 90°, 0°)	(0°, 0°, 0°)	(0°, 0°, 0°)

Table 4

The simulation parameters for Figure 8 (see Table 1 for explanation).

4.7	4.1	4.5
(0.5, 0.5)	(−0.1, −0.1)	(−0.5, −0.5)
(32, 1)	(35, 1)	(33, 1)
(0°, 0°, 0°)	(0°, 0°, 0°)	(0°, 0°, 0°)
3.4	4.1	4.6
(0.5, 0.5)	(−0.1, −0.1)	(−0.5, −0.5)
(35.5, 1)	(35.5, 1)	(35.5, 1)
(90°, 0°, 0°)	(90°, 0°, 0°)	(90°, 0°, 0°)
3.9	3.9	5.1
(−1, 0)	(−0.5, 0)	(−1, 0)
(35,1)	(35, 1)	(35, 1)
(0°, 0°, 0°)	(0°, 0°, 0°)	(90°, 0°, 0°)

Table 5

The simulation parameters for Figure 9 (see Table 1 for explanation).

0 (−0.2, −0.2) (0, 0) (0°, 0°, 0°)	0 (−0.2, −0.2) (5, 0) (0°, 0°, 0°)	0 (−0.2, −0.2) (10, 0) (0°, 0°, 0°)
0 (−0.2, −0.2) (20, 0) (0°, 0°, 0°)	0 (−0.2, −0.2) (40, 0) (0°, 0°, 0°)	0 (−0.2, −0.2) (40, 0) (90°, 0°, 0°)

Table 6

Sets of *hfi* constants $\mathbf{A} = (A_x, A_y, A_z)$ estimated from analysis of HYSCORE spectra at g_x, g_y and g_z, and the isotropic *hfi* constants a_{iso} and the anisotropic *hfi* constants $\mathbf{T} = (T_x, T_y, T_z)$ estimated from $\mathbf{A}$. The sets differ by the choice of the relative signs of the different components of $\mathbf{A}$.

Set No.	(A_x, A_y, A_z) [MHz]	a_{iso} [MHz]	(T_x, T_y, T_z) [MHz]
I	±(3.9, 2.9, 4.3)	±3.7	±(0.2, −0.8, 0.6)
II	±(−3.9, 2.9, 4.3)	±1.1	±(−5.0, 1.8, 3.2)
III	±(3.9, −2.9, 4.3)	±1.8	±(2.1, −4.7, 2.5)
IV	±(3.9, 2.9, −4.3)	±0.8	±(3.1, 2.1, −5.13)